Thermomechanically and Conformationally Consistent Coarse-Graining of Donor-Acceptor Polymers via Energy-Renormalization Approach

Yang Wang,[†,‡] Zhaofan Li,[¶] Andrea Giuntoli,[*,†] and Wenjie Xia[*,¶]

†*Zernike Institute for Advanced Materials, University of Groningen, 9747 AG, Groningen, The Netherlands*

‡*Department of Theoretical Physics & Center for Biophysics, Saarland University, 66123 Saarbrücken, Germany*

¶*Department of Aerospace Engineering, Iowa State University, Ames, IA 50011, United States*

E-mail: a.giuntoli@rug.nl; wxia@iastate.edu

Abstract

Understanding the thermomechanical and conformational properties of semiconducting donor-acceptor conjugated polymers (D-A CPs) at a fundamental molecular scale is essential for designing high-performance devices. However, the substantial computational demands of all-atom (AA) simulations and the complex heterogeneous structures of CPs pose significant challenges in thoroughly investigating the properties of CPs approaching real devices scale. Herein, leveraging the well-established framework of the energy-renormalization (ER) approach, we develop a temperature- and architecture-transferable, chemistry-specific coarse-grained (CG) model for polydiketopyrrolopyrrole (PDPP)-based D-A CPs with significantly improved computational efficiency. Our results show excellent agreement between AA and CG simulations in predicting key properties such as density, Debye-Waller factors, and Young's modulus across a wide temperature range and chain architectures. Specifically, the ER-corrected CG model captures trends in glass transition temperature (T_g) and mechanical properties, aligning closely with experimental data. The CG model reveals that longer sidechain lengths and less bulky backbone conjugation units induce lower T_g and Young's modulus, with bulky backbone units exhibiting slower dynamics. The localization model accurately predicts relaxation times across different molecular architectures. Additionally, the CG model's conformational properties align with experimental data and theoretical worm-like chain models, showing that persistence length increases with longer sidechains, while bulky backbone moieties decrease it. These findings deepen our understanding of the complex interactions between flexible sidechains and rigid backbones in CPs with diverse architectures, offering important insights for the strategic design of CPs with tailored properties.

Keywords: Molecular dynamics simulations; coarse-graining; energy renormalization; conformation; dynamics; mechanical properties

INTRODUCTION

Conjugated polymers (CPs), featuring a monomer structure characterized by a relatively stiff conjugated backbone and a flexible side chain, are a kind of semiconducting materials and show remarkable potential in organic electronic devices, like organic solar cells (OSCs),[1] organic field-effect transistors (OFETs),[2] and stretchable and ultra-flexible wearable devices[3,4] due to their intrinsic advantages, including flexibility, lightweight, and inexpensive solution processability.[5] Therefore, the thermomechanical properties are equally critical compared with the electronic properties when CPs are utilized for fabricating advanced stretchable and flexible electronic devices and wearable electronics.[6,7] Over past decades, the third-generation semiconducting polymers of donor-acceptor (D-A) CPs with more complex molecular structures in the repeat unit, especially the polydiketopyrrolopyrrole (PDPP)-based D-A CPs,[8,9] have attracted tremendous attention for their low band gap, controllable electronic and thermomechanical properties at the most fundamental molecular level through backbone and sidechain engineering approaches.[10–13] Additionally, DPPT-based D-A CPs eliminate the need for extra acceptor or donor additives for efficient charge transport, leading to simpler, more efficient, and more durable devices. However, due to the inherent complexity and diversity in the molecular structure of D-A CPs' building blocks, experimental measurement of their thermomechanical response presents significant challenges, necessitating a specific modeling and computational predictive framework to predict the thermomechanical properties of D-A CPs.

Computational approaches, particularly atomistically-informed coarse-grained (CG) simulations, offer a promising avenue to explore the thermomechanical behavior,[7,14–16] self-assembly,[17,18] and morphology associated charge mobility and electronic properties[17,19,20] of CPs at extended spatiotemporal scales by eliminating unnecessary degrees of freedom and capturing the essential features of CPs in the all-atom (AA) representation. Regarding thermomechanical properties, the three-site CG model of poly(3-hexylthiophene) (P3HT), one of the most well-understood CPs, has been carefully parameterized and extensively uti-

lized for the solution, nanocomposite and thin-film systems.[7,16,21] However, the systematical chemistry-specificity CG modeling of third-generation D-A CPs remains notably deficient, largely because of their intricate chemical structures and a large number of different interactions.[22] Reisjalali et al.[23] introduced a hybrid equilibration approach for DPPT-based semiconducting polymers, employing CG and full atomistic resolutions for the alkyl side chains and backbone, respectively. Their findings indicate that the back-mapping method can generate equilibrated structures with reduced computational cost but the thermomechanical and dynamic behavior of DPPT-based CPs are not incorporated.

The iterative Boltzmann inversion (IBI) method is a leading technique for developing the CG model and relative CG interactions based on the underlying AA model.[24] However, the configurational entropy (s_c) is inevitably lost upon coarse-graining,[25] yielding a smoother energy landscape and insufficient atomistic frictional forces in the CG resolution,[26] further causing artificially accelerated dynamics,[27] overpredicted diffusive behavior,[28] and softer mechanical response.[29] Importantly, the general CG models are always derived at specific thermodynamic states, significant deviations in density and diffusion coefficient arise when transitioning the system to different temperatures.[19] To address these issues, we propose a dynamically consistent CG modeling strategy, known as energy renormalization (ER), aimed at accurately capturing the temperature-dependent dynamics of the desired glass-forming systems. Drawing inspiration from the Adam-Gibbs (AG) theory[30] and the generalized entropy theory (GET),[31] the ER strategy compensates the s_c loss upon coarse-graining by renormalizing the enthalpy of the CG system (*i.e.*, 'enthalpy-entropy compensation' effect) through tuning the van der Waals interaction energy (cohesive energy) of the CG system, which is parametrically linked to the nonbonded interaction parameter ϵ in the Lennard-Jones (LJ) potential.[32] A large body of literature has proved the strong correlation between cohesive energy and various dynamic properties such as diffusion,[33] relaxation time,[34,35] tensile, and shear modulus[16,36] in glass-forming materials. Although the ER method has demonstrated efficacy in coarse-grained modeling across various polymer species,[16,25,32,37,38]

its application to polymer systems with heterogeneous structures of D-A CPs remains relatively unexplored. The challenges lie in the complex and heterogeneous structures of the backbones and sidechains of novel DPPT-based D-A CPs. These complexities result in markedly different properties between the backbone and sidechain, such as conformation and dynamics, with their interplay predominantly influencing the behavior of the materials. DPPT-based CPs often exhibit significant conformational flexibility that influences their electronic properties. Therefore, accurate representation of chain conformations, mechanical behavior, and thermodynamic stability requires deliberate modeling approaches.

In the present work, we employ the ER protocol to develop the chemistry-specificity CG model of polydiketopyrrolopyrrole (PDPP)-based D-A CPs composing heterogeneous structures with varied alkyl side-chain lengths and backbone moieties for the first time (**Figure 1**). Specifically, we introduce the ER factor $\alpha(T)$ and $\beta(T)$ for the energy parameter ϵ and length-scale parameter σ in the LJ potential by matching the Debye-Waller factor (DWF) $\langle u^2 \rangle$ and density of the AA model to the CG model as a function of temperature, yielding the temperature-transferable CG model that further captures the dynamical and conformational behaviors with different molecular architectures. Results demonstrated that the initial estimations of cohesive interaction strength ϵ and effective length parameter σ could be directly obtained based on the geometry of cluster of atoms regarding the complex molecular architectures, simplifying the parameterization procedure and demonstrating the versatility and practicability of the ER method. The cohesive energy shows a prominent effect on the dynamics and mechanical behavior of the CG model by conducting the calculation of segmental relaxation time and tensile deformation. Results confirmed the experimental trend that T_g and E decrease with longer side chains and increase with the more bulky donors incorporated in the backbone. Similarly, the PDPP-based CPs with shorter side chain lengths or containing more thiophene ring moieties in the backbone exhibit more suppressed dynamics. Overall, our simulation results show the ability of the ER method to efficiently and accurately capture the mechanical and dynamical behavior of D-A CPs

with varying side chain lengths and backbone moieties over a wide temperature range. We also highlight the important role of side-chain and backbone structures in influencing the conformational behaviors of D-A CPs under molecular scale, offering an effective strategy to theoretically design and predict the dynamics and thermomechanical properties of future new D-A polymers.

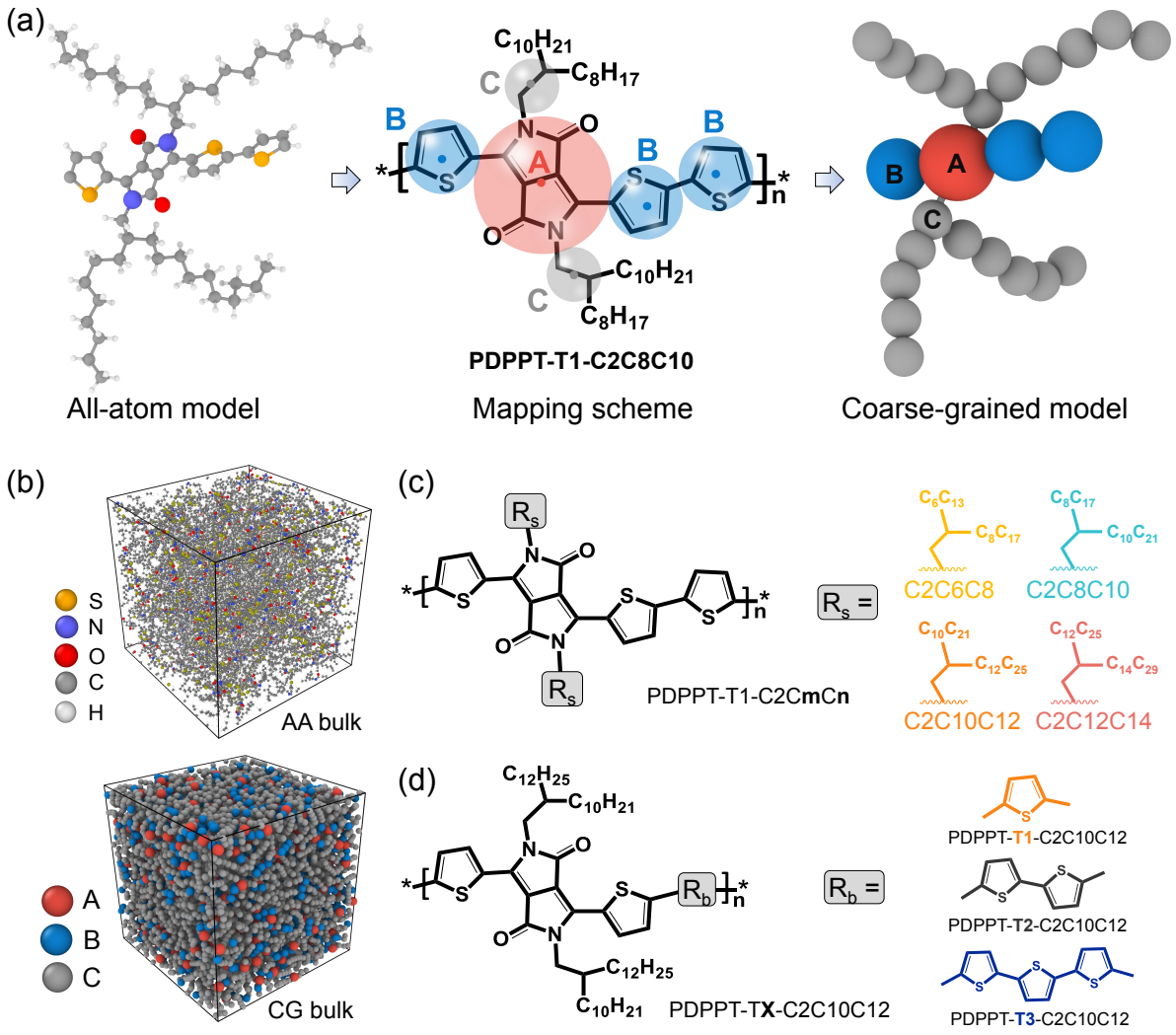

Figure 1. Coarse-grained mapping scheme of PDPP-based conjugated polymers. (a) Coarse-grained model of one monomer of conjugated polymer PDPPT-T1-C2C8C10, showing the mapping from (left) all-atomistic (AA) model to (right) coarse-grained (CG) model. (Middle) Each repeat unit is represented by three bead types, *i.e.*, A, B, and C, the force centers of CG beads are located at the center-of-mass of the DPP core, thiophene ring, and two adjacent carbons with bonded hydrogen atoms. (b) The snapshots of the equilibrated amorphous PDPPT-T1-C2C8C10 bulk AA and CG systems. (c) Chemical structure of PDPPT-T1-C2C**m**C**n** with different side chain lengths, where $\boldsymbol{m}$ and $\boldsymbol{n}$ indicate the number of carbon atoms in the two branched alkyl chains, respectively, *i.e.*, $\boldsymbol{n} = \boldsymbol{m} + 2$. (d) Chemical structure of PDPPT-T**X**-C2C10C12 with **X** denoting the number of isolated thiophene rings in the backbone of each monomer.

MODEL AND METHODS

The Materials Studio platform is used to build the all-atomistic (AA) model of PDPP-based polymers with the side chain attached to the DPP core, as shown in **Figure 1**a. One single AA PDPPT- T1-C2C8C10 chain with 40 repeating units (6122 atoms) is initially packed into one big box based on the Python package pysimm.[39] It is noted that the complex molecular architecture of PDPP-based CPs comprises abundant atoms within one monomer or chain, making atomistic investigation insufficient for comprehensive analysis, particularly when considering bulk systems. The Dreiding force field and Gasteiger method are adopted to calculate bonded (including bond, angle, and dihedral) and nonbonded interactions (vdW and electrostatic) in the AA system. An energy minimization is first performed using the conjugate gradient algorithm.[40] Then, the system is equilibrated in the melt state at a high T of 1000 K under the NPT ensemble for 1.5 ns with the pressure ramping from 1 to 800 atm. Next, the system is cooled down to the target temperature with a cooling rate of 0.2K/ps and pressure gradually decreasing to 1 atm under the NPT ensemble. It is noted that the annealing process is performed for every individual temperature case. Finally, a 2 ns equilibration dynamics run under an NPT ensemble is conducted to collect the atomistic trajectories with a sampling interval of 1 ps. The periodic boundary conditions are applied in all three directions to eliminate the surface effect. The CG molecular dynamics simulation follows the same procedure above. For each CG system, we insert 50 polymer chains with 10 monomers per chain into the simulation box, yielding a box size of $10\times10\times10$ nm^3. The Nose/Hoover barostat and thermostat are applied to control the temperature and pressure of the system. The timesteps of 1 and 4 fs are used for the AA and CG simulations, respectively. Accordingly, the temperature-damping and pressure-damping parameters are 100 fs and 1000 fs, 400 fs and 4000 fs for AA and CG models, respectively. We utilize single AA and CG polymer chains to derive the bonded probability distribution functions required for determining CG bonded interactions, ensuring computational efficiency. Previous work has declared that the bonded interactions will not influenced by the chain length (molec-

ular weight).[41] We conduct AA simulations for PDPP-based CPs with different molecular structures depicted in **Figure 1**c and d to get the average bonded probability distributions. Subsequently, the simulation of bulk systems containing multiple chains follows the same simulation strategy outlined above.

Properties calculation

According to previous studies, the $\langle u^2 \rangle$ quantifies the molecular "free volume" and "stiffness" in the picosecond time.[25] We regard $\langle u^2 \rangle$ as the mean-square displacement (MSD) value of all CG beads at around t ≈ 4 ps, a time scale related to caging estimated from our simulations, calculated by

$$\left\langle r^2(t) \right\rangle = \frac{1}{N} \sum_{j=1}^{N} \left[\boldsymbol{r}_j(t) - \boldsymbol{r}_j(0) \right]^2 \tag{1}$$

where $\boldsymbol{r}_j(t)$ is the position of the center of mass of the j_{th} bead at time t, N denotes the total number of CG beads, and the angular brackets denote the ensemble average. The segmental relaxation time τ is calculated by the intermediate scattering function $F_s(\boldsymbol{q}, t)$

$$F_s(q,t) = \frac{1}{N} \sum_{1}^{N} exp\left\{ -i\boldsymbol{q} \cdot \left[\boldsymbol{r}_j(t) - \boldsymbol{r}_j(0) \right] \right\} \tag{2}$$

where $\boldsymbol{q}$ is the wave vector that is taken from the first peak position of the structure factor $S(q)$ as shown in Supporting **Figure S12**, and $\boldsymbol{r}_j(t)$ is the coordinate of particle j at time t. The relaxation time τ is determined as the time when $F_s(q,t)$ decays to $1/e$,[42] as shown in **Figure S13**. The tensile stress and modulus E are calculated via atomic virial stress tensor:

$$\sigma_{xy} = -\frac{1}{V} \left[\sum_{i}^{N} m_i (\boldsymbol{v}_i)_x (\boldsymbol{v}_i)_y + \sum_{i>j}^{N} \frac{\partial U}{\partial r_{ij}} \frac{(\boldsymbol{r}_{ij})_x (\boldsymbol{r}_{ij})_y}{\boldsymbol{r}_{ij}} \right] \tag{3}$$

where V and U denote the volume and total energy of the system, $\boldsymbol{r}_{ij}$ denotes the distance between particles i and j, m, and v are the mass and velocity of the particle. During the

stretch, we survey the polymer chain orientation using the orientation order parameter P_2:

$$P_2 = \left\langle \frac{3 * cos^2\theta - 1}{2} \right\rangle \tag{4}$$

where θ is the angle between an arbitrary bond vector (all bonds) and the deformation direction, including the x, y, and z directions for improving statistical accuracy, $\langle ... \rangle$ denotes the ensemble average. All the simulations, including AA and CG simulations, are achieved using the LAMMPS software package.[43] The visualization is performed using OVITO software.[44] The trajectory analysis is realized using an object-oriented Python toolkit MDAnalysis (https://www.mdanalysis.org).[45]

RESULTS AND DISCUSSION

Molecular Design and CG Modeling

To examine the influence of side-chain and backbone on the thermodynamic and mechanical properties of CPs, we systematically select four and three PDPP-based polymers featuring different side-chain lengths and backbone moieties based on previous experiment works.[8,11] Specifically, four increased side-chain lengths, ranging from C2C6C8 (2-hexyl decyl) to C2C8C10 (2-octyl dodecyl), and from C2C10C12 (2-decyl tetradecyl) to C2C12C14 (2-dodecyl hexadecyl) are appended to the DPP core; three moieties of thiophene (T), bithiophene (T2), and terthiophene (T3) are incorporated for the DPP core in the backbone, as illustrated in **Figure 1**c,d. To develop the atomistically informed CG model of PDPP-based CPs, we apply three CG bead types to represent one monomer structure, *i.e.*, bead A for the DPP core, bead B for thiophene ring, and bead C for two consecutive carbons in the side chain accompanied with the covalently bonded hydrogen atoms (middle panel of **Figure 1**a). **Figure 1**b shows the representative snapshots of equilibrated AA and CG systems of PDPPT-T1-C2C8C10. The force center is located at the center of mass of all atoms under-

lying each CG bead. With this mapping scheme, we can easily expand the coarse-grained (CG) model to include other PDPP-based conjugated polymers (CPs) with diverse chemical structures by incorporating CG beads B and C for the backbone and side chains. It is important to acknowledge that the CG mapping scheme employed in our model is not unique and can vary based on different factors. In our CG model, the DPP core is represented as a single bead, designated as bead A, which is considerably larger compared to beads B and C. This size disparity is attributed to the planar structure of the DPP core, which results in a relatively smaller loss of configurational entropy upon coarse-graining. This strategic representation is essential for accurately capturing the system's physical properties and dynamic behaviors within our CG model while minimizing the complexity of the CG force field.

Bonded Interaction Optimization

Based on the defined CG mapping scheme, the target bonded probability distributions can be directly obtained through AA simulation. Notably, the averaged probability distribution functions are obtained based on PDPPT-T**X**-C2C8C10 models with varying backbone structures. Then, the effective CG bonded potentials are derived after 7-9 iterations with the iterative Boltzmann inversion (IBI) method:

$$U_{i+1}(x) = U_i(x) + k_B T ln \left[\frac{P_i(x)}{P_{target}(x)} \right] \tag{5}$$

where k_B is the Boltzmann constant and T is the absolute temperature; the variable x refers to the bond length l, bond angle θ, dihedral angle ϕ, and improper dihedral χ, respectively; $P_i(x)$ represents the relative probability distribution in i_{th} iteration; $P_{target}(x)$ denotes the target probability distribution derived directly from AA simulation. **Figure 2** shows the representative average probability distributions of the bonds, angles, dihedrals, and improper of three PDPPT-T**X**-C2C8C10 CPs with different backbone structures. The other bonded parts are elaborated in **Figures S1** and **S2**. The CG potentials are derived with IBI based

on the average probability distribution and the final bonded interaction CG parameters are summarized in **Table S1**.

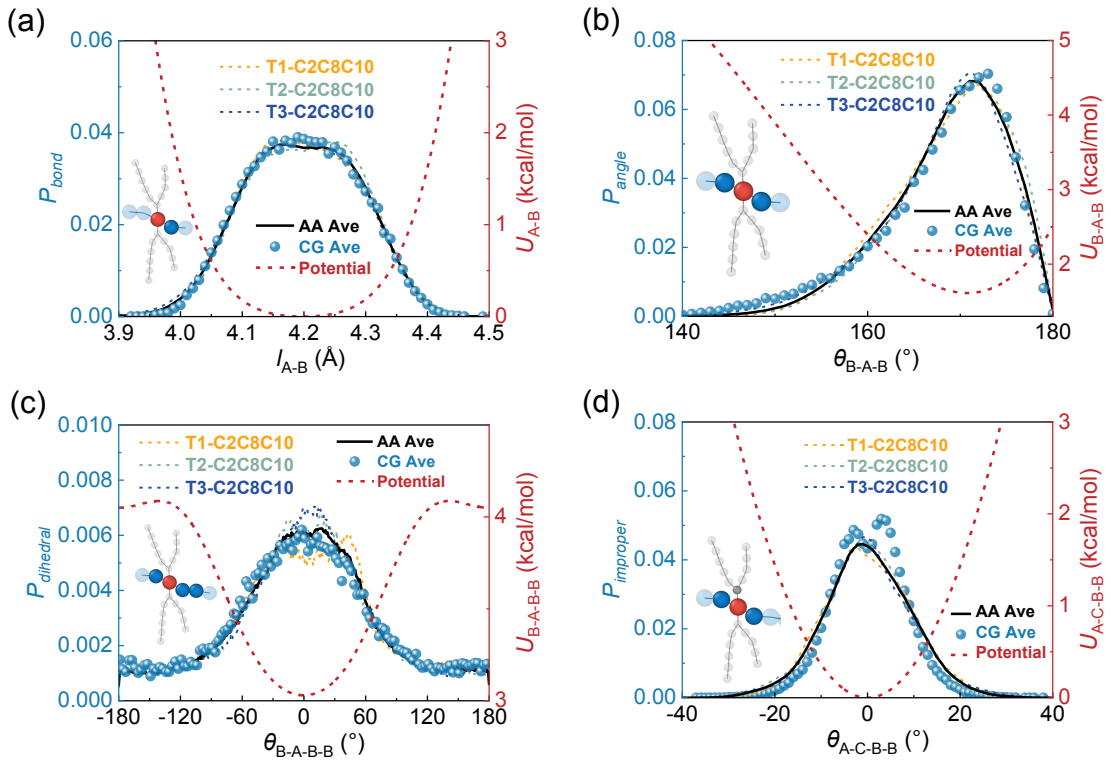

Figure 2. The representative averaged probability distribution functions of the (a) A-B bond, (b) B-A-B angle, (c) B-A-B-B dihedral, and (d) A-C-B-B improper for AA and CG PDPPT-T**X**-C2C8C10 models at 300 K, the red dotted lines denote the corresponding CG bonded potentials.

Nonbonded Interaction Optimization

For describing the nonbonded interactions of different CG beads, we employ a commonly applied GROMACS style 12-6 Lennard-Jones (LJ) potential for its simplicity and computational efficiency in describing intra- and intermolecular nonbonded interactions:

$$U_{lj}(r) = \begin{cases} 4\epsilon \left[\left(\frac{\sigma}{r}\right)^{12} - \left(\frac{\sigma}{r}\right)^{6} \right], & r < R_{inner} \\ S_{LJ}(r), & R_{inner} < r < R_{outer} \end{cases} \tag{6}$$

where σ governs the effective van der Waals radius and marks the radial distance where the potential crosses the zero energy line, and ϵ is the depth of the potential well depth in energy units associated with the cohesive interaction strength of the materials. The energy switching function S_{LJ} is used in CG simulation to smoothly ramp the energy to zero between inner cutoff R_{inner} = 12 Å and outer cutoff R_{outer} = 15 Å. The CG model considers six different parameters for nonbonded interactions: σ_{11} and ϵ_{11} LJ parameters for the DPP core and DPP core interactions; σ_{22} and ϵ_{22} for the thiophene and thiophene ring interactions; σ_{33} and ϵ_{33} for the sidechain ethyl and ethyl interactions. The cross-interaction terms are taken as the arithmetic average for $\sigma_{ij} = (\sigma_{ii}+\sigma_{jj})/2$ and the geometric average for $\epsilon_{ij} = \sqrt{\epsilon_{ii}\epsilon_{jj}}$, respectively, where i and j denote different particle species. To achieve temperature transferability, we employ the energy-renormalization approach and introduce temperature rescaling factors $\beta(T)$ and $\alpha(T)$ for σ and ϵ, respectively. Specifically, the effective LJ parameters σ and ϵ are treated as a function of T: $\sigma_{ii}(T) = \beta(T)\sigma_{ii}^0$ and $\epsilon_{ii}(T) = \alpha(T)\epsilon_{ii}^0$, where σ_{ii}^0 and ϵ_{ii}^0 are the initial estimates of nonbonded interaction. In the previous works,[16,25] the initial estimation of σ_{ii}^0 and ϵ_{ii}^0 is obtained from the radial distribution function (RDF), $g(r)$, of the CG force centers based on the direct Boltzmann inversion: $U_{nonbonded}^0(r) = -k_BTln[g(r)]$. However, due to the complex chemical structure of DPPT-based CP, the RDF curves of backbone beads (A and B) show multiple peaks, which can hardly be fitted to get a reasonable initial estimate. Previous work utilized a large ϵ value for the CG bead in the chain end with a large size.[46] Similarly, we employed radius ratio and mass ratio methodologies to derive an initial estimate of σ and ϵ for the DPPT backbone beads (type A and B) as a starting point based on our previous ER modeling of P3HT,[16] which will be refined in subsequent analyses. The detailed procedures for obtaining initial estimates of ϵ and σ are elaborated in **Figures S3** and **S4** in **Supporting Information**. Here, we note that the essence of the ER method involves rescaling the enthalpy (ϵ) of the CG system to compensate for the entropy loss during coarse-graining, which, in turn, leads to reduced accuracy in reproducing the local structure of atomistic chains (RDF) due to the

shift of the nonbonded potential.[25]

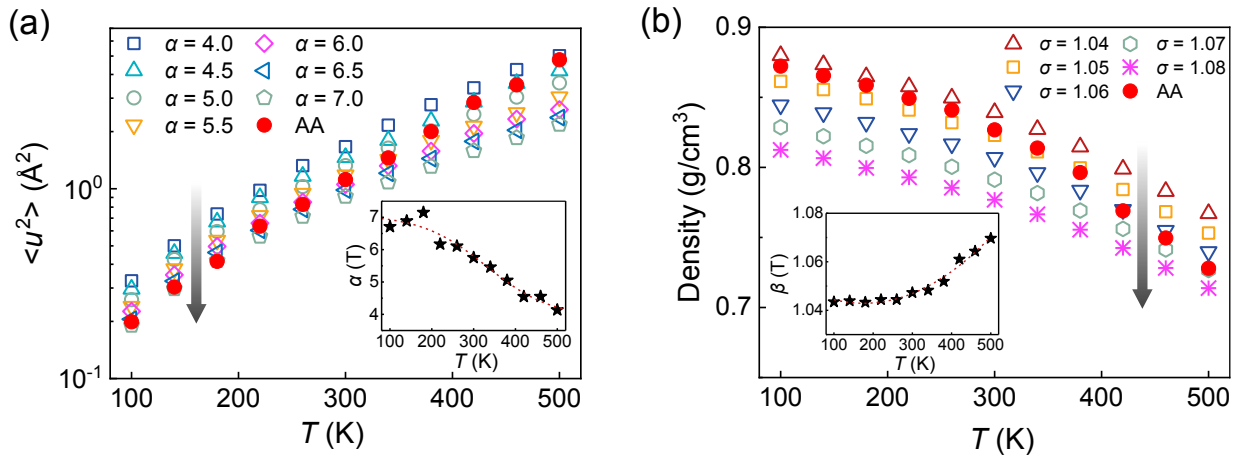

Figure 3. Calibrations of ER factors of $\boldsymbol{\alpha(T)}$ and $\boldsymbol{\beta(T)}$ based on PDPPT-T1-C2C8C10. (a) The Debye-Waller factor $\langle u^2 \rangle$ as a function of temperature for AA and CG models of PDPPT-T1-C2C8C10 with varying α parameters for cohesive interaction strength. Inset: The $\alpha(T)$ curve for the CG model is determined by preserving the T-dependent $\langle u^2 \rangle$ of the AA model of PDPPT-T1-C2C8C10. (b) Density as a function of T for the AA and CG models of PDPPT-T1-C2C8C10 with varying β parameters controlling the interaction length scale. Inset: The $\beta(T)$ curve for the CG model is determined by capturing the T-dependent density of the AA model of PDPPT-T1-C2C8C10. The red solid circle represents the target $\langle u^2 \rangle$ and densities of the PDPPT-T1-C2C8C10 AA model at different temperatures. The vertical arrow denotes a dataset with an increase in α and β, respectively.

Energy renormalization approach

Previous works have demonstrated the potential of the ER approach in developing temperature-transferable CG models of polymer.[16,25] The ER method utilizes the localization model (LM) of relaxation of glass formation (GF), providing a scaling relationship between relaxation time (τ) and the short time scale dynamics of GF liquids (Debye-Waller factor, DWF), *i.e.*, $\tau \sim \exp(u_0^2/\langle u^2 \rangle)$ (u_0^2 is a constant). The classical free volume theory of τ correlates relaxation time with free volume through a simple exponential relationship, $\tau = \tau_0 \cdot \exp(v_0/v_f)$, where v_f is the "free volume". Simple dimensional consistency suggests that v_f should scale with the $\langle u^2 \rangle$ as $v_f \sim \langle u^2 \rangle^{3/2}$, yielding the equation $\tau = \tau_0 \cdot \exp[(u_0^2/\langle u^2 \rangle)^{3/2}]$. Given the anisotropic shape of the dynamical free volume regions and the inherent anisotropy of intermolecular potential interactions in molecules, Simmons et

al.[47] provided a more general scaling relationship $v_f \sim \langle u^2 \rangle^{\alpha/2}$, thus $\tau = \tau_0 \cdot \exp[(u_0^2/\langle u^2 \rangle)^{\alpha/2}]$. Subsequently, Betancourt et al.[48] provided a more predictive relationship between $\tau \sim \langle u^2 \rangle$ by normalizing u_0^2 with its value $u_A^2 \equiv \langle u^2(T_A) \rangle$ at the onset temperature T_A for molecular caging and obtained:

$$\tau(T) = \tau_A \cdot \exp\left[\left(u_A^2/\left\langle u^2(T)\right\rangle\right)^{\alpha_0/2} - 1\right] \tag{7}$$

where τ_A and u_A^2 are the relaxation time and DWF at onset temperature, α_0 is the only empirical fitting parameter and correlated to the free volume shape.[32] For the specific case of isotropic free volume, the localization model anticipates $\alpha_0 = 3$.[48] In our simulations, the $\langle u^2 \rangle$ is determined from the mean-squared displacement (MSD) $\langle r^2(t) \rangle$ of the center of mass of monomers in the AA and CG models at around t $\approx$ 4 ps, corresponding to the caging dynamics. The onset temperature T_A is identified as the temperature of GF where particle caging first emerges and below which relaxation becomes non-Arrehenius. Specifically, T_A signals the onset of non-Arrhenius behavior of τ_α and can be obtained by characterizing the temperature at which τ departs from the Arrhenius regime. The determination of T_A for the PDPPT-T1-C2C6C8 CG model is shown in **Figure S9**a in the **Supporting Information**.

The LM declares that by preserving $\langle u^2 \rangle$ between CG and AA models, the segmental dynamics can be maintained. As the ER method suggested, the temperature-dependent ER factor of $\alpha(T)$ is introduced for the cohesive energy (ϵ) in LJ potential as a function of temperature, *i.e.*, $\epsilon(T) = \alpha(T)\epsilon_0$, where ϵ_0 is the initial estimate and elaborated in the **Supporting Information**. By systematically tuning the α over a wide temperature range, the $\langle u^2 \rangle$ data of the CG model covers that of the AA model (**Figure S5**). As shown in **Figure 3**a, the $\langle u^2 \rangle$ increases with elevating temperature for all α values and decreases with increasing α at certain temperatures, indicating the dynamics (mobility) of the polymer chain are suppressed under low temperature and high cohesive energy. The $\alpha(T)$ is then obtained using the interpolation method based on $\langle u^2 \rangle$ under different α values and temperatures

(inset in **Figure 3**a), which is well described using a sigmoidal function

$$\alpha(T) = \frac{\alpha_A - \alpha_G}{1 + \exp\left[-k(T - T_T)\right]} + \alpha_G \tag{8}$$

where α_G and α_A denote the α in the glassy and Arrhenius regime, respectively, k is a parameter related to the temperature breadth of the transition and T_T refers to the crossover point of this sigmoidal function. Similarly, the ER factor of $\beta(T)$ is introduced for the length scale parameter $\sigma(T)$ in LJ potential to preserve the structural properties such as density, *i.e.*, $\sigma(T) = \beta(T) \cdot \sigma_0$, where σ_0 is the initial estimate and elaborated in the **Supporting Information**. As shown in **Figure 3**b, the function form of $\beta(T)$ is determined as $\beta(T) = \beta_2 T^2 + \beta_1 T + \beta_0$. The parameters of ER factor $\alpha(T)$ and $\beta(T)$ are summarized in the **Table 1**.

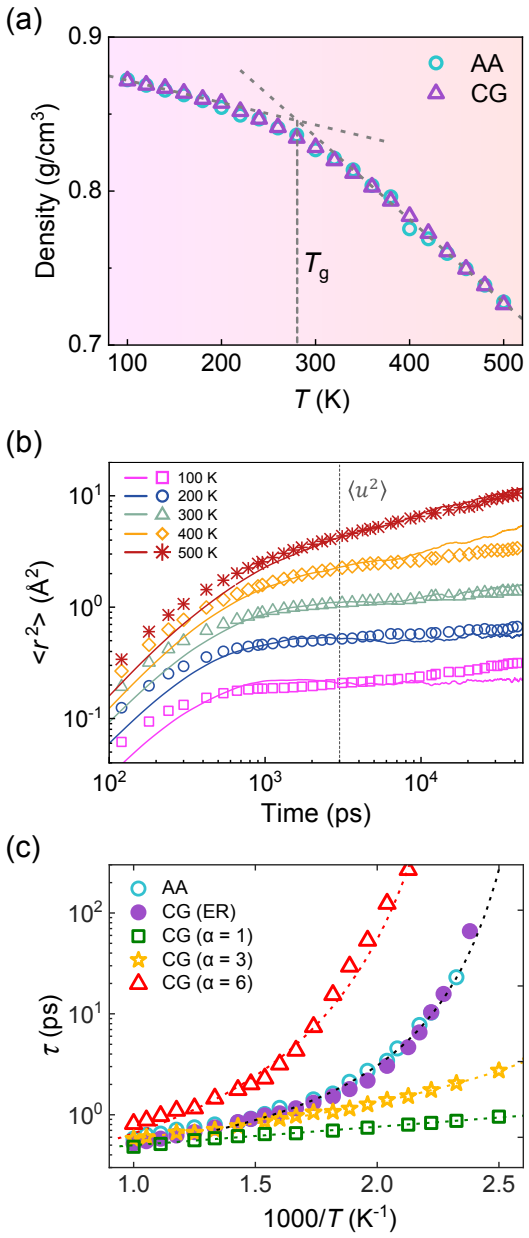

Figure 4. Comparison of structural properties and dynamics of PDPPT-T1-C2C8C10 AA and CG models over a wide temperature range. (a) The density versus T curve of AA and ER-corrected CG models. The intersection of two linear fittings of high and low T regimes are determined as glass transition temperature, T_g. (b) MSD curves versus simulation time for the AA (line) and CG (symbol) models. The vertical dashed line refers to the time when $\langle u^2 \rangle$ is determined. (c) Segmental relaxation time, τ, as a function of temperature for the AA and CG models. The open and solid circle markers represent the τ data for the AA and ER-corrected CG models, respectively. The squares are the segmental relaxation time of a model generated with the initial estimates of ϵ_0 and σ_0 (without ER). The stars and triangles denote the CG model with a constant ER factor of α. The dashed lines represent the VFT fits of τ data.

Table 1. Nonbonded Interactions of PDPP-based D-A Conjugated Polymers CG Model and Energy-Renormalization Function with Parameters of $\alpha(T)$ and $\beta(T)$.

ER functional forms	Parameters
$E_{LJ}(r,T) = 4\epsilon(T)\left\{\left[\frac{\sigma(T)}{r}\right]^{12} - \left[\frac{\sigma(T)}{r}\right]^{6}\right\} + S_{LJ}(r)$	$\epsilon_{AA} = \alpha(T) \times 3.862 \times 10^{-1}$ kcal/mol, $\sigma_{AA} = \beta(T) \times 7.843$ Å $\epsilon_{BB} = \alpha(T) \times 2.400 \times 10^{-1}$ kcal/mol, $\sigma_{BB} = \beta(T) \times 4.219$ Å $\epsilon_{CC} = \alpha(T) \times 8.873 \times 10^{-2}$ kcal/mol, $\sigma_{CC} = \beta(T) \times 4.842$ Å
$\alpha(T) = \frac{\alpha_A - \alpha_G}{1+\exp[-k(T-T_T)]} + \alpha_G$	$\alpha_A = 3.888$, $\alpha_G = 7.087$, $k = 1.275 \times 10^{-2}$ K^{-1}, $T_T = 330.6$ K
$\beta(T) = \beta_2 T^2 + \beta_1 T + \beta_0$	$\beta_2 = 2.603 \times 10^{-7}$ K^{-2}, $\beta_1 = -9.142 \times 10^{-5}$ K^{-1}, $\beta_0 = 1.051$

Using the derived ER factors $\alpha(T)$ and $\beta(T)$, we proceed to characterize the density and dynamics of the PDPPT-T1-C2C8C10 CG model. **Figure 4**a illustrates the density variation with temperature for the AA and CG models, indicating that the T-dependent ER factor of $\beta(T)$ can faithfully capture the density of the target AA model across a broad temperature range. As the CG model faithfully reproduces the density of the target AA model, we could obtain the glass transition temperature (T_g) by combining AA and CG data. The crossover of linear fits in the glassy and Arhennius regimes determines T_g as 289.3 K, which is about 23 K higher than the experimental T_g (266.5 K) for the PDPPT-T1-C2C8C10 obtained by dynamic mechanical analysis and could be attributed to the fast cooling rate in MD simulation.[49] We next examine the dynamics of the CG model based on $\langle r^2(t)\rangle$ over a wide temperature range. **Figure 4**b shows the comparison of the $\langle r^2(t)\rangle$ for the AA (lines) and CG (symbols) models at different temperatures, highlighting the efficacy of the ER method in capturing the $\langle r^2(t)\rangle$ curves of the AA model over at different temperatures. However, slight deviations of $\langle r^2(t)\rangle$ persist due to the coexistence of CG beads with varying sizes and cohesive energies in the system, which may cause a wider range of caging scales and relaxation times.[38] The comparison of $\langle u^2\rangle$ for the AA and CG models at T spanning from the high-T Arrhenius regime to the low-T glassy regime is depicted in **Figure S5**. Additionally, the heterogeneous chain architectures of PDPP-based CPs lead to distinct dynamics for the backbone and sidechain. **Figure S6** systematically analyzes the dynamics of the backbone, sidechain, and individual bead species of the PDPPT-T1-C2C8C10 CG system, revealing that the backbone's mobility is slower than that of the sidechain, with

backbone bead A (DPP core) exhibiting the slowest dynamics in the system. For a more comprehensive theoretical background on this rescaling method, we encourage readers to refer to our previous works.[25,37] **Figure 4**c demonstrates the segmental relaxation time τ of AA and CG PDPPT-T1-C2C8C10 models by evaluating the intermediate scattering function $F_s(q,t)$. Results show a fair consistency in τ for the AA and ER-corrected CG model, which can be well described using the well-known Vogel-Fulcher-Tammann (VFT) equation that expresses the temperature-dependent relaxation behavior as $\tau(T) = \tau_0 \cdot \exp(DT_0/(T - T_0))$, where τ_0, D, and T_0 are fitting constants that describe relaxation process of GF (**Figure 4**c). Furthermore, T_g can be estimated by extrapolating τ to the empirical observation time scale, *i.e.*, $\tau(T_g) \approx 100\ s$,[50] where the T_g is determined as 297.6 K. It is noted that the predicted T_g from the VFT relation is a rough estimate and exceeds those obtained from experiments and **Figure 4**a due to the high sensitivity of extrapolation to minor data perturbations. To test the effect of cohesive energy on the τ, we use a constant ER factor α near the high-T Arrhenius regime ($\alpha = 3$) and the low-T glassy regime ($\alpha = 6$), respectively. The τ based on the initial estimate of ϵ ($\alpha = 1$) is also calculated for comparison. As shown in **Figure 4**c, a fixed α value shows severe discrepancy in capturing τ, especially in the low-T range, substantiating the indispensability of utilizing the ER method in preserving the T-dependent relaxation behavior of GF. In addition, the results indicate that the ER-corrected CG model of PDPP-based CPs achieves a 100-fold improvement in computational efficiency over the AA counterpart, as illustrated in **Figure S7**.

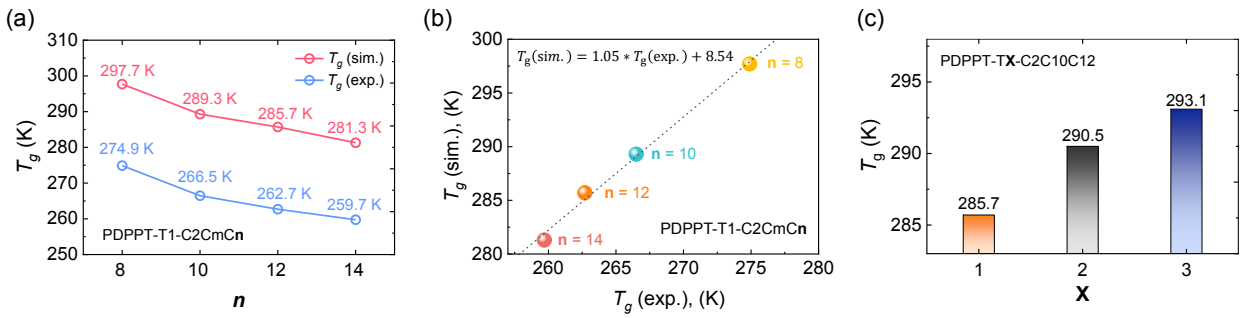

Figure 5. Glass transition temperatures of PDPP-based CPs. (a) Glass transition temperatures of PDPPT-T1-C2C**m**C**n** CPs with different side-chain lengths from CG-MD simulation and experimental.[11] (b) A predictive linear relationship between experimental and simulated glass transition temperatures of PDPPT-T1-C2C**m**C**n** CPs. (c) Glass transition temperatures of PDPPT-T**X**-C2C10C12 CPs with different thiophene rings in the backbone from CG-MD simulation.

To test the predictability of CG models for other PDPP-based CPs with varying side-chain lengths and different numbers of thiophene rings in the backbone, we introduce beads B and C to the backbone and side chains, respectively. **Figure S8** illustrates that for PDPP-based CPs, an increase in side-chain length correlates with a reduction in density at a given temperature, whereas an increase in the number of thiophene rings in the backbone corresponds to an elevation in density. **Figure 5**a reveals a decline in T_g as the side-chain length of PDPPT-T1-C2C**m**C**n** polymer increases, manifesting a consistent trend with the experiment, although with a deviation of 23 K higher than the experimental values due to the fast cooling rate in MD. Soldera et al.[51] provided a predictive linear relationship obtained between experimental and simulated $T_g s$ of vinylic polymers, which in our work is derived as $T_g(sim.) = 1.05 * T_g(exp.) + 8.54$ (**Figure 5**b). As for the PDPPT-T**X**-C2C10C12 CPs, the T_g increases with more thiophene rings (B beads) incorporated into the backbone (**Figure 5**c), in good agreement with the backbone T_g of PDPP-based CPs in previous experiment work.[13] It is important to note that the results in **Figure 5**c are based on PDPP-based CPs with a consistent number of monomers, specifically 10 monomers per chain. However, this results in varying chain lengths due to the different numbers of thiophene rings in each monomer. To eliminate the effect of chain length, we examined the T_g of PDPPT-T**X**-

C2C10C12 CPs, ensuring the same chain length by adjusting the number of monomers per chain. As shown in **Figure S14**, the T_g values are identical in both cases. Overall, our results show that the CG model in this work can capture the T_g trend of PDPP-based CPs with different chain structures although the value is higher than the experiment. As PDPP-based CPs have a high-T_g backbone with slow dynamics and a low-T_g side chain with faster dynamics, such heterogeneous chain properties cause multiple T_g and make it difficult to accurately capture T_g.[10,52,53] Additionally, different experiment probing methods could also lead to different T_g values.[8]

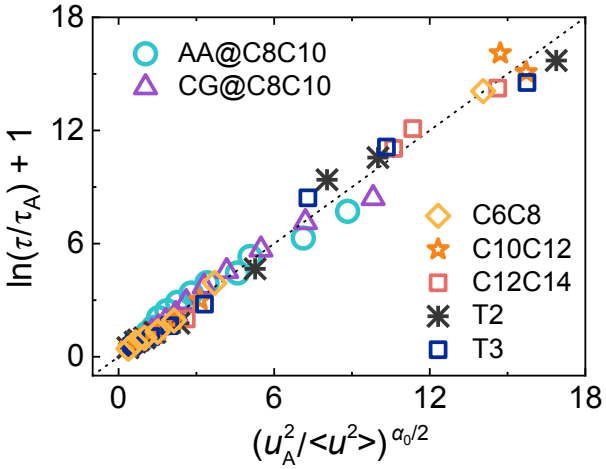

Figure 6. Test of the localization model predictions of τ for the AA and CG models via **Eq 7**. The linear collapse of relaxation time (τ) vs. Debye-Waller factor ($\langle u^2 \rangle$) data for the AA (circle) and CG (triangle) PDPPT-T1-C2C8C10 models, with other PDPP-based CPs CG models with different molecular architecture are also included for comparison.

We next test the relaxation behavior of PDPP-based CPs with different molecular structures in **Figure S9** in **Supporting Information**. Results indicate that longer side-chain lengths result in lower τ value, signifying faster system dynamics. Conversely, an increased number of thiophene rings (bead B) in the backbone leads to a higher τ value, which aligns with the mobility analysis of each bead type (**Figure S6**). To test the localization model for τ of the PDPP-based CPs with various molecular structures under different temperatures, we apply **Eq. 7** to quantitatively describe our simulation results. **Figure 6** illustrates the scaling relationship between τ and $\langle u^2 \rangle$ for both AA and CG models of PDPPT-T1-C2C8C10

and other CG models of CPs with different chain architectures, showing that all data converge onto a master curve. Our ER approach successfully reproduces the scaling relationship between the $\langle u^2 \rangle$ and τ for the AA model across a broad temperature range (**Figure 6**). The exponent α_0 for each CG model is approximately 2.59 ± 0.14, as detailed in **Supporting Information Figure S10**. This value is consistent with our previous ER research on P3HT ($\alpha_0 = 2.7$), suggesting that the 'caging' regions formed by the surrounding molecules are irregular, likely due to the influence of the flexible bottlebrush-like side chain on the local free volume. It is observed that the α_0 value increases from 2.62 to 3.86 as chain stiffness increases from previous work,[54] indicating that greater chain stiffness leads to a reduction in the anisotropy of free volume. In our model, given the minimal differences in molecular structure, the α_0 value does not exhibit significant variation. However, CPs with a greater number of thiophene rings result in increased polymer backbone stiffness,[8] corresponding to higher values, as seen in the cases of T2 and T3 CPs ($\alpha_0 = 2.77$).

The mechanical properties, such as Young's modulus, toughness, and stiffness, are crucial for CPs in the applications of flexible devices.[11,14] Herein, based on the ER-corrected CG model, we examine the thermomechanical properties and the effects of stretching on chain conformation in PDPP-based CPs. **Figure 7**a shows snapshots of the PDPPT-T1-C2C8C10 bulk system before and after stretching to 160%, where only the backbones are shown and apparent chain alignment along the tensile direction is detected via P_2 (**Figure 7**d). Remarkably, the ER-corrected CG model faithfully reproduces the stress-strain curve of the target AA model although its Young's modulus (1.75 GPa) is higher than the experimentally measured value of 0.3 GPa obtained using the 'film-on-water' stretching method. The overestimation of Young's modulus in both the AA and CG models can be attributed to the high strain rate used in the simulation due to the computational limitations. Zhang et al[55] observed the strain rate-dependent mechanical properties of PDPP-based CPs free-standing thin film in experiments, where an increase of elastic modulus is detected with increasing strain rate. In addition, molecular weight (M_n) and dispersity also affect mechanical prop-

erties and require further investigation.[56] As discussed in previous works,[21,57] $1/\langle u^2 \rangle$ can be regarded as a measure of molecular stiffness and correlated to mechanical properties via $E \approx A + B/\langle u^2 \rangle$, where A and B are fitting parameters. Therefore, we characterize the mechanical properties and DWF for the PDPP-based CPs with different molecular architectures in **Figure 7**c, where an apparent power-law relationship is observed, which is consistent with the P3HT bulk system.[16] In addition, we quantify the anisotropic structural changes of the polymer chains during the stretching test using the axial and transverse components of the radius of gyration and end-to-end distance. **Figure 7**d illustrates the evolution of the axial and transverse components of P_2 and ΔR_{ee} as a function of strain. Both quantities indicate increasing chain alignment along the stretching direction with rising strain. The chain alignment parameter calculated here can be linked to the experimentally accessible 2D Herman's orientation parameter of the material: $P_{||} = (R-1)/(R+1)$, where R is the dichroic ratio. Gu et al.[9] reported a value of approximately 0.14 for the chain alignment parameter for the PDPPT-T1-C2C8C10 film strained to 59%, while an enhanced orientation parameter of 0.36 was detected at the same strain (59%) using the 'film-on-elastomer' method, which is comparable with our simulation value of 0.20 at 59% strain. **Figure 7**e illustrates the evolution of the radius-of-gyration (ΔR_g) during tensile deformation, highlighting the expansion of polymer chains under tensile deformation.

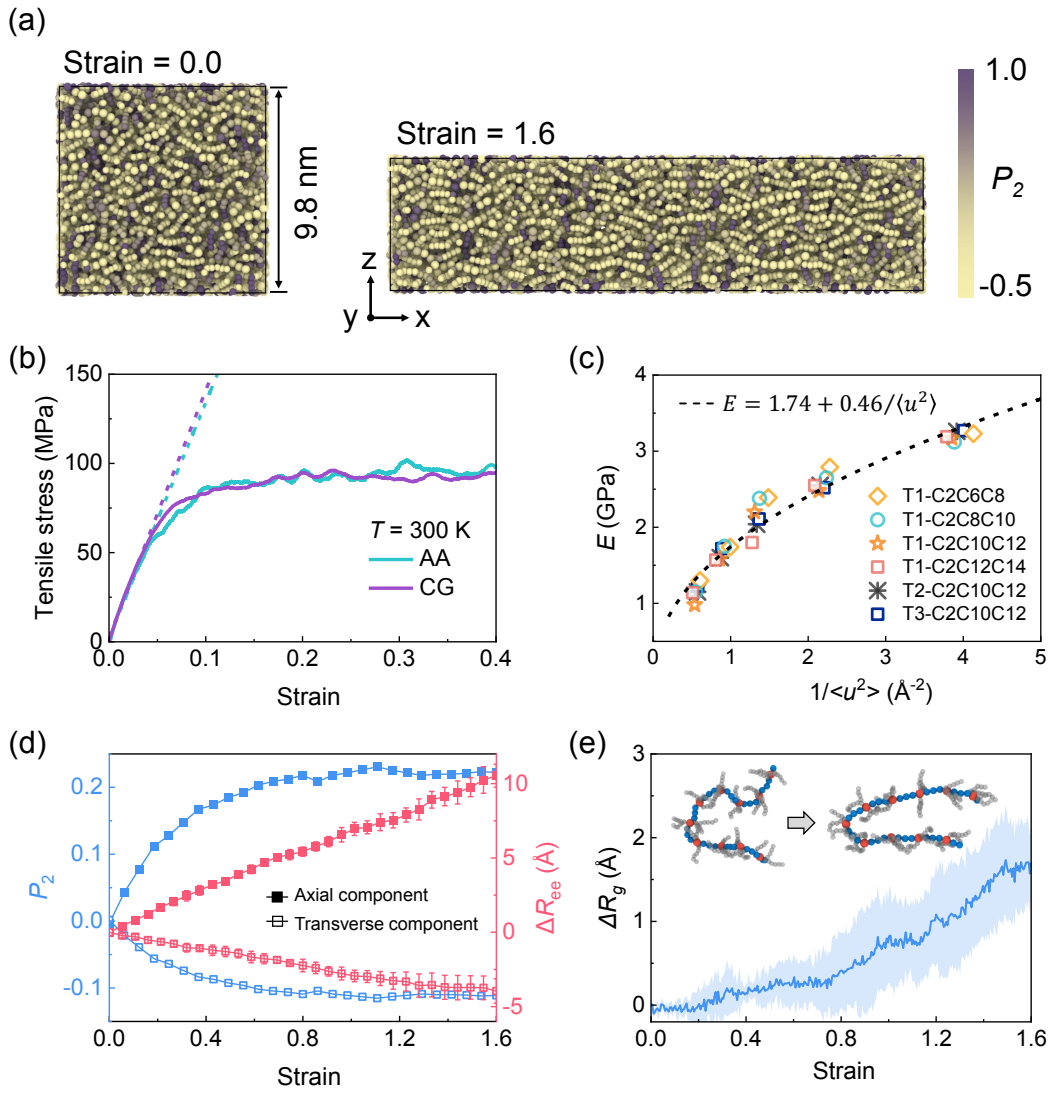

Figure 7. Thermomechanical properties of PDPPT-T1-C2C8C10 bulk system. (a) Representative snapshots showing a cross-section of the simulated morphology before and after straining to 160% (only backbones are shown here for clarity). The color map denotes the bond order parameter P_2 via **eq. 4**. (b) Stress-strain curves of PDPPT-T1-C2C8C10 AA and CG models with dashed lines represent the linear fitting of the elastic stage for obtaining Young's modulus. (c) Tensile modulus E vs. molecular stiffness $1/\langle u^2 \rangle$ of the PDPP-based CPs with various molecular architectures at different temperatures. (d) The evolution of the axial and transverse components of the chain alignment parameter, P_2, and the change of end-to-end distance, ΔR_{ee} during stretching. (e) The evolution of the change of radius of gyration, ΔR_g, during the uniaxial loading simulation.

Table 2. Chain Conformation of PDPP-based D-A Conjugated Polymers with 15 Monomers per Chain from MD Simulation and Wormlike Chain Model.

Polymer	l_p (nm)	L_c (nm)	$\langle R_g^2 \rangle$ (nm^2)	$\langle R_g^2 \rangle_{WLC}$ (nm^2)	$\langle R_e^2 \rangle$ (nm^2)	$\langle R_e^2 \rangle_{WLC}$ (nm^2)
T1-C2C6C8	12.6	23.7	38.1 ± 0.2	33.5	433.6 ± 19.1	327.8
T1-C2C8C10	13.5	23.7	37.2 ± 0.3	34.2	426.8 ± 15.1	338.0
T1-C2C10C12	15.6	23.7	39.6 ± 1.3	35.5	403.6 ± 4.8	358.8
T1-C2C12C14	23.7	23.7	36.3 ± 0.7	38.8	383.0 ± 1.0	412.8
T2-C2C10C12	5.4	29.4	34.5 ± 1.0	33.2	227.2 ± 37.9	263.9
T3-C2C10C12	7.2	35.4	57.0 ± 1.2	50.2	362.4 ± 55.7	408.9

Chain conformation

To investigate chain conformation based on the ER-corrected CG model, we constructed a large simulation box with 200 chains (15 monomers per chain) randomly incorporated in the system at an extremely low density of 0.0001 g/cm^3, resulting in 84,000 CG beads within the PDPPT-T1-C2C10C12 system, equivalent to approximately 531,100 atoms in AA resolution, posing computational challenges. It is noted that the CG system for conformation study is different from the melt system for mechanical test. A cut-and-shifted LJ potential is used to describe the nonbonded interactions between CG beads for mimicking a good solvent [58]

$$U_{lj}(r) = \begin{cases} 4\epsilon \left[(\frac{\sigma}{r})^{12} - (\frac{\sigma}{r})^{6} + \frac{1}{4} \right], & r < 2^{1/6}\sigma \\ 0, & r \geq 2^{1/6}\sigma \end{cases} \tag{9}$$

where ϵ and σ refer to the cohesive energy and distance parameter between two CG beads (**Table 2**). The LJ cutoff = $2^{1/6}\sigma$ results in purely repulsive interactions between particles. The system was first equilibrated for 0.8 ns under a canonical (NVT) ensemble with a time step of 4 fs. After equilibration, the simulations were subjected to a 2 ns production run in the NVT ensemble, and the data were collected every 4 ps to sample configurational trajectories adequately. The periodic boundary condition (PBC) was applied to all three

directions.

Several measures characterize DPPT-based CPs' conformation: persistence length l_p, mean-square end-to-end distance $\langle R_e^2 \rangle$, and mean-square radius-of-gyration $\langle R_g^2 \rangle$. Persistence length is a frequently used measure to describe the chain stiffness of the polymer chain. In MD simulation, l_p is defined as the length at which two points on the polymer backbone become decorrelated and determined by measuring the autocorrelation $C(n)$ of two bond vectors ($\boldsymbol{a}_i$,$\boldsymbol{a}_{i+n}$) separated by n bonds[59]

$$C(n) = \langle cos\theta_{i,\, i+n} \rangle = \langle \boldsymbol{a}_i \cdot \boldsymbol{a}_{i+n} \rangle \approx e^{-\frac{n \cdot \bar{l_B}}{l_p}} \tag{10}$$

where $\bar{l_B}$ is the average bond length of the backbone and determined from MD simulations to be $\sim$ 4.0 Å based on the different DPPT-based CPs in this work, and n is the number of backbone beads (beads A and B). The statistical behavior of chain conformations is determined by the ratio of the l_p to the contour length L_c. Specifically, when $l_p \ll L_c$, the polymer chain behaves like a flexible coil; when $l_p \gg L_c$, the polymer behaves like a rigid rod; for the $l_p \approx L_c$, polymers are semiflexible and can be described as wormlike chains (WLC). It is well known that third-generation D-A CPs are typical semiflexible polymers, which can be well described using the most appropriate WLC model.[60] The mean-square end-to-end distance $\langle R_e^2 \rangle$ and mean-square radius-of-gyration $\langle R_g^2 \rangle$ are two quantities to measure the chain shape, which can be derived from MD simulation and the WLC model, respectively[59,61]

$$\langle R_g^2 \rangle_{WLC} = \frac{1}{3} l_p L_c - l_p^2 + 2\frac{l_p^3}{L_c} \left\{ 1 - \frac{l_p}{L_c} \left[1 - \exp(-\frac{L_c}{l_p}) \right] \right\} \tag{11}$$

$$\langle R_e^2 \rangle_{WLC} = 2l_p^2 \left[\frac{L_c}{l_p} - 1 + \exp\left(-\frac{L_c}{l_p} \right) \right] \tag{12}$$

where L_c is the counter length of the polymer chain, *i.e.*, $L_c = (n-1) \cdot \bar{l_B}$. The chain conformation information of l_p, $\langle R_g^2 \rangle$, $\langle R_e^2 \rangle$ of PDPP-based CPs with varying lengths of side chains and different numbers of thiophene rings in the backbone can be obtained from MD

simulation and the results are summarized in **Table 2**. Taking PDPPT-T1-C2C10C12 CP as an example, we demonstrated in **Figure S11** how to obtain the l_p, $\langle R_g \rangle$, and $\langle R_e \rangle$. It is noted that the $\left\langle R_g^2 \right\rangle_{MD}$ shows a subtle influence based on the backbone or whole chain (**Figure S11b**). Results show that the PDPPT-T1-C2C10C12 possesses a l_p of 15.6 nm, comparable with previous experiment data of 18.1 nm obtained using the small-angle neutron scattering technique.[49] Additionally, the l_p and $\langle R_e^2 \rangle_{MD}$ of DPPT-T1-C2C**m**C**n** increase and decrease as the side-chain length (**m** and **n**) increases, where l_p follows the relation of $l_p \sim N_{sc}^{9/8}$ (**Figure S11**d), which is slightly different from previous work declaring that the l_p of linear poly(vinyl alcohol)-graft-poly(ethylene oxide) follows a relation of $l_p \sim N_{sc}^{15/8}$, where N_{sc} is the side-chain length.[62] As the number of thiophenes moieties increases, the conjugated backbone becomes more flexible since l_p becomes smaller than DPPT-T1-C2C10C12 (the l_p decreasing from 15.6 nm for PDPPT-T1-C2C10C12 to 5.4 nm for PDPPT-T2-C2C10C12 and 7.2 nm for PDPPT-T3-C2C10C12). It is also noted that Hsu et al. demonstrated that the l_p increases as the L_c increases for the bottle-brush polymer.[63] Overall, the conformational results of the $\left\langle R_g^2 \right\rangle$ and $\langle R_e^2 \rangle$ from the MD simulation are in good agreement with the experimental results and the WLC model.

CPs have made significant strides in recent decades, showcasing remarkable versatility characterized by their highly tunable rigid conjugation backbones and flexible sidechains, which can be well described in our CG model. The versatility of CPs allows precise modulation of chemical structures to optimize various properties. Therefore, more attention might be paid to future computational research on D-A CPs with diverse and complex structures based on our CG model, such as naphthalenediimide (NDI) and isoindigo (IID) based CPs.[64–67] Although current CG models primarily focus on chain-level properties of bulk amorphous D-A CPs, some semicrystalline domains may also be present.[65,68,69] To advance this field, future studies could explore a broader range of properties, such as thermal, self-assembly, optical, and electronic characteristics, by integrating CG model development with machine learning for material property prediction, which could uncover unprecedented

functionalities and applications and drive novel innovations and breakthroughs.

CONCLUSIONS

In conclusion, this study developed a temperature- and architecture-transferable CG model of PDPP-based CPs. The CG model faithfully captures the density, dynamic, mechanical, and conformational properties compared to the target AA model and experimental data with different molecular architectures and temperatures. By adjusting $\langle u^2 \rangle$ (fast dynamics physical property at a picosecond time scale) as a function of temperature through renormalization cohesive energy parameter ϵ with $\alpha(T)$, the CG model captures the dynamics of the AA model over a wide temperature range. Surprisingly, the ER-corrected CG model successfully captures the mechanical properties of the target AA model by accurately reproducing the stress-strain curves, though it does overestimate Young's modulus compared to experimental results. The reason is that AA simulations overestimate the modulus due to the higher strain rate and our CG model is calibrated based on the target AA model. Importantly, the ER-corrected CG model also predicts the conformational behavior of DPP-based CPs with different molecular architectures in the implicit good solvent, which aligns well with the worm-like chain theoretical model. This is crucial for understanding the conformation-related electrical properties of CPs. However, due to the isotropic nature of the CG modeling, *i.e.*, the conjugated moieties are treated as spherical beads, and their planar nature is neglected, precise measurement of electric properties remains challenging. Therefore, employing an anisotropic model for CPs,[70] such as treating conjugated moieties as plates and more precise quantum chemistry calculations could better address this issue. Additionally, aspects such as backbone and side-chain architectures, molecular weight, temperature, and the impact of side-chain on overall dynamics and chain conformation are potential interesting topics for future research, which our current modeling work could not fully explore due to space limitations. Ultimately, our work demonstrates the effectiveness and applicability

of the ER approach in developing a multiscale, temperature- and architecture-transferable modeling framework for CPs with various molecular structures. This framework can be readily applied to other CPs sharing the same building blocks of conjugated moieties and alkyl side chains, providing a robust approach to understanding semiconducting materials at the fundamental molecular scale.

Acknowledgement

Y.W. and A.G. thank the Center for Information Technology of the University of Groningen for their support and for providing access to the Hábrók high-performance computing cluster. Z. Li and W. Xia acknowledge the support from the National Science Foundation (NSF) under NSF CMMI Award No. 2237063 and the Department of Aerospace Engineering at Iowa State University.

Supporting Information Available

The Supporting Information is available free of charge at https://...

Bonded and nonbonded interactions characterization (**Figures S1-S4**); Dynamics characterization (**Figures S5-S6**); Computational efficiency (**Figure S7**); Thermodynamics of the CG PDPP-based CPs (**Figures S8-S10**); Conformation behavior (**Figure S11**); Structure factor (**Figure S12**); Intermediate scatter function (**Figure S13**); Glass transition temperature comparison (**Figure S14**); Bonded Parameters for CG Model of PDPP-based D-A Conjugated Polymers (**Table S1**).

References

(1) Holliday, S.; Ashraf, R. S.; Wadsworth, A.; Baran, D.; Yousaf, S. A.; Nielsen, C. B.; Tan, C. H.; Dimitrov, S. D.; Shang, Z.; Gasparini, N.; Alamoudi, M.; Laquai, F.; Brabec, C. J.; Salleo, A.; Durrant, J. R.; McCulloch, I. High-efficiency and air-stable P3HT-based polymer solar cells with a new non-fullerene acceptor. *Nat. Commun.* **2016**, *7*, 11585.

(2) Liu, Y.; Hao, W.; Yao, H.; Li, S.; Wu, Y.; Zhu, J.; Jiang, L. Solution Adsorption Formation of a π-Conjugated Polymer/Graphene Composite for High-Performance Field-Effect Transistors. *Adv. Mater.* **2018**, *30*, 1705377.

(3) Wang, S.; Oh, J. Y.; Xu, J.; Tran, H.; Bao, Z. Skin-Inspired Electronics: An Emerging Paradigm. *Acc. Chem. Res.* **2018**, *51*, 1033–1045.

(4) Koo, J.; Amoli, V.; Kim, S. Y.; Lee, C.; Kim, J.; Park, S.-M.; Kim, J.; Ahn, J. M.; Jung, K. J.; Kim, D. H. Low-power, deformable, dynamic multicolor electrochromic skin. *Nano Energy* **2020**, *78*, 105199.

(5) Liu, C.; Shao, L.; Chen, S.; Hu, Z.; Cai, H.; Huang, F. Recent progress in π-conjugated polymers for organic photovoltaics: solar cells and photodetectors. *Prog. Polym. Sci.* **2023**, 101711.

(6) Alesadi, A.; Cao, Z.; Li, Z.; Zhang, S.; Zhao, H.; Gu, X.; Xia, W. Machine learning prediction of glass transition temperature of conjugated polymers from chemical structure. *Cell Rep. Phys. Sci.* **2022**, *3*, 100911.

(7) Root, S. E.; Savagatrup, S.; Pais, C. J.; Arya, G.; Lipomi, D. J. Predicting the mechanical properties of organic semiconductors using coarse-grained molecular dynamics simulations. *Macromolecules* **2016**, *49*, 2886–2894.

(8) Zhang, S.; Ocheje, M. U.; Huang, L.; Galuska, L.; Cao, Z.; Luo, S.; Cheng, Y.-H.; Ehlenberg, D.; Goodman, R. B.; Zhou, D.; others The critical role of electron-donating thiophene groups on the mechanical and thermal properties of donor-acceptor semiconducting polymers. *Adv. Electron. Mater.* **2019**, *5*, 1800899.

(9) Zhang, S.; Alesadi, A.; Mason, G. T.; Chen, K.; Freychet, G.; Galuska, L.; Cheng, Y.; St. Onge, P. B. J.; Ocheje, M. U.; Ma, G.; Qian, Z.; Dhakal, S.; Ahmad, Z.; Wang, C.; Chiu, Y.; Rondeau-Gagné, S.; Xia, W.; Gu, X. Molecular Origin of Strain-Induced Chain Alignment in PDPP-Based Semiconducting Polymeric Thin Films. *Adv. Funct. Mater.* **2021**, *31*, 2100161.

(10) Galuska, L. A.; McNutt, W. W.; Qian, Z.; Zhang, S.; Weller, D. W.; Dhakal, S.; King, E. R.; Morgan, S. E.; Azoulay, J. D.; Mei, J.; others Impact of backbone rigidity on the thermomechanical properties of semiconducting polymers with conjugation break spacers. *Macromolecules* **2020**, *53*, 6032–6042.

(11) Zhang, S.; Alesadi, A.; Selivanova, M.; Cao, Z.; Qian, Z.; Luo, S.; Galuska, L.; Teh, C.; Ocheje, M. U.; Mason, G. T.; St. Onge, P. B. J.; Zhou, D.; Rondeau-Gagné, S.; Xia, W.; Gu, X. Toward the Prediction and Control of Glass Transition Temperature for Donor–Acceptor Polymers. *Adv. Funct. Mater.* **2020**, *30*, 2002221.

(12) Wang, G. N.; Gasperini, A.; Bao, Z. Stretchable Polymer Semiconductors for Plastic Electronics. *Adv. Electron. Mater.* **2018**, *4*, 1700429.

(13) Zheng, Y.; Zhang, S.; Tok, J. B.-H.; Bao, Z. Molecular design of stretchable polymer semiconductors: current progress and future directions. *J. Am. Chem. Soc.* **2022**, *144*, 4699–4715.

(14) Root, S. E.; Savagatrup, S.; Printz, A. D.; Rodriquez, D.; Lipomi, D. J. Mechanical properties of organic semiconductors for stretchable, highly flexible, and mechanically robust electronics. *Chem. Rev.* **2017**, *117*, 6467–6499.

(15) Yoshimoto, Y.; Sugiyama, S.; Shimada, S.; Kaneko, T.; Takagi, S.; Kinefuchi, I. Molecular insights into the mechanical properties of polymer–fullerene bulk heterojunctions for organic photovoltaic applications. *Macromolecules* **2021**, *54*, 958–969.

(16) Wang, Y.; Li, Z.; Niu, K.; Xia, W. Energy renormalization for coarse-graining of thermomechanical behaviors of conjugated polymer. *Polymer* **2022**, *256*, 125159.

(17) Lee, C. K.; Hua, C. C.; Chen, S. A. Phase transition and gels in conjugated polymer solutions. *Macromolecules* **2013**, *46*, 1932–1938.

(18) Schwarz, K. N.; Kee, T. W.; Huang, D. M. Coarse-grained simulations of the solution-phase self-assembly of poly (3-hexylthiophene) nanostructures. *Nanoscale* **2013**, *5*, 2017–2027.

(19) Jones, M. L.; Huang, D. M.; Chakrabarti, B.; Groves, C. Relating Molecular Morphology to Charge Mobility in Semicrystalline Conjugated Polymers. *J. Phys. Chem. C* **2016**, *120*, 4240–4250.

(20) Simine, L.; Allen, T. C.; Rossky, P. J. Predicting optical spectra for optoelectronic polymers using coarse-grained models and recurrent neural networks. *Proc. Natl. Acad. Sci. U. S. A.* **2020**, *117*, 13945–13948.

(21) Wang, Y.; Li, Z.; Sun, D.; Jiang, N.; Niu, K.; Giuntoli, A.; Xia, W. Understanding the thermomechanical behavior of graphene-reinforced conjugated polymer nanocomposites via coarse-grained modeling. *Nanoscale* **2023**, *15*, 17124–17137.

(22) Heeger, A. J. Semiconducting polymers: the Third Generation. *Chem. Soc. Rev.* **2010**, *39*, 2354–2371.

(23) Reisjalali, M.; Manurung, R.; Carbone, P.; Troisi, A. Development of hybrid coarse-grained atomistic models for rapid assessment of local structuring of polymeric semiconductors. *Mol. Syst. Des. Eng.* **2022**, *7*, 294–305.

(24) Reith, D.; Pütz, M.; Müller-Plathe, F. Deriving effective mesoscale potentials from atomistic simulations. *J. Comput. Chem.* **2003**, *24*, 1624–1636.

(25) Xia, W.; Song, J.; Jeong, C.; Hsu, D. D.; Phelan, J., F. R.; Douglas, J. F.; Keten, S. Energy-Renormalization for Achieving Temperature Transferable Coarse-Graining of Polymer Dynamics. *Macromolecules* **2017**, *50*, 8787–8796.

(26) Kmiecik, S.; Gront, D.; Kolinski, M.; Wieteska, L.; Dawid, A. E.; Kolinski, A. Coarse-grained protein models and their applications. *Chem. Rev.* **2016**, *116*, 7898–7936.

(27) Meinel, M. K.; Müller-Plathe, F. Loss of molecular roughness upon coarse-graining predicts the artificially accelerated mobility of coarse-grained molecular simulation models. *J. Chem. Theory Comput.* **2020**, *16*, 1411–1419.

(28) Fritz, D.; Koschke, K.; Harmandaris, V. A.; van der Vegt, N. F.; Kremer, K. Multiscale modeling of soft matter: scaling of dynamics. *Phys. Chem. Chem. Phys.* **2011**, *13*, 10412–10420.

(29) Rosch, T. W.; Brennan, J. K.; Izvekov, S.; Andzelm, J. W. Exploring the ability of a multiscale coarse-grained potential to describe the stress-strain response of glassy polystyrene. *Phys. Rev. E* **2013**, *87*, 042606.

(30) Adam, G.; Gibbs, J. H. On the temperature dependence of cooperative relaxation properties in glass-forming liquids. *J. Chem. Phys.* **1965**, *43*, 139–146.

(31) Dudowicz, J.; Freed, K. F.; Douglas, J. F. Generalized entropy theory of polymer glass formation. *Adv. Chem. Phys.* **2008**, *137*, 125.

(32) Xia, W.; Hansoge, N. K.; Xu, W.-S.; Phelan Jr, F. R.; Keten, S.; Douglas, J. F. Energy renormalization for coarse-graining polymers having different segmental structures. *Sci. Adv.* **2019**, *5*, eaav4683.

(33) Song, J.; Hsu, D. D.; Shull, K. R.; Phelan Jr, F. R.; Douglas, J. F.; Xia, W.; Keten, S. Energy renormalization method for the coarse-graining of polymer viscoelasticity. *Macromolecules* **2018**, *51*, 3818–3827.

(34) Xu, W.-S.; Douglas, J. F.; Freed, K. F. Influence of Cohesive Energy on the Thermodynamic Properties of a Model Glass-Forming Polymer Melt. *Macromolecules* **2016**, *49*, 8341–8354.

(35) Xu, W.-S.; Douglas, J. F.; Xia, W.; Xu, X. Understanding Activation Volume in Glass-Forming Polymer Melts via Generalized Entropy Theory. *Macromolecules* **2020**, *53*, 7239–7252.

(36) Alesadi, A.; Xia, W. Understanding the role of cohesive interaction in mechanical behavior of a glassy polymer. *Macromolecules* **2020**, *53*, 2754–2763.

(37) Xia, W.; Song, J.; Hansoge, N. K.; Phelan Jr, F. R.; Keten, S.; Douglas, J. F. Energy renormalization for coarse-graining the dynamics of a model glass-forming liquid. *J. Phys. Chem. B* **2018**, *122*, 2040–2045.

(38) Giuntoli, A.; Hansoge, N. K.; van Beek, A.; Meng, Z.; Chen, W.; Keten, S. Systematic coarse-graining of epoxy resins with machine learning-informed energy renormalization. *npj Comput. Mater.* **2021**, *7*, 168.

(39) Fortunato, M. E.; Colina, C. M. pysimm: A python package for simulation of molecular systems. *SoftwareX* **2017**, *6*, 7–12.

(40) Payne, M. C.; Teter, M. P.; Allan, D. C.; Arias, T. A.; Joannopoulos, J. D. Iterative minimization techniques for ab initio total-energy calculations: molecular dynamics and conjugate gradients. *Rev. Mod. Phys.* **1992**, *64*, 1045–1097.

(41) Zhang, X.-Z.; Lu, Z.-Y.; Qian, H.-J. Temperature transferable and thermodynamically consistent coarse-grained model for binary polymer systems. *Macromolecules* **2023**, *56*, 3739–3753.

(42) Mishra, C. K.; Ma, X.; Habdas, P.; Aptowicz, K. B.; Yodh, A. Correlations between short-and long-time relaxation in colloidal supercooled liquids and glasses. *Phys. Rev. E* **2019**, *100*, 020603.

(43) Plimpton, S. Fast Parallel Algorithms for Short-Range Molecular Dynamics. *J. Comp. Phys.* **1995**, *117*, 1–19.

(44) Stukowski, A. Visualization and Analysis of Atomistic Simulation Data with OVITO-the Open Visualization Tool. *Modell. Simul. Mater. Sci. Eng.* **2010**, *18*, 015012.

(45) Michaud-Agrawal, N.; Denning, E. J.; Woolf, T. B.; Beckstein, O. MDAnalysis: a toolkit for the analysis of molecular dynamics simulations. *J. Comput. Chem.* **2011**, *32*, 2319–27.

(46) Uehara, S.; Wang, Y.; Ootani, Y.; Ozawa, N.; Kubo, M. Molecular-level elucidation of a fracture process in slide-ring gels via coarse-grained molecular dynamics simulations. *Macromolecules* **2022**, *55*, 1946–1956.

(47) Simmons, D. S.; Cicerone, M. T.; Zhong, Q.; Tyagi, M.; Douglas, J. F. Generalized localization model of relaxation in glass-forming liquids. *Soft Matter* **2012**, *8*, 11455–11461.

(48) Pazmiño Betancourt, B. A.; Hanakata, P. Z.; Starr, F. W.; Douglas, J. F. Quantitative relations between cooperative motion, emergent elasticity, and free volume in model glass-forming polymer materials. *Proc. Natl. Acad. Sci. U.S.A.* **2015**, *112*, 2966–2971.

(49) Cao, Z.; Tolba, S. A.; Li, Z.; Mason, G. T.; Wang, Y.; Do, C.; Rondeau-Gagné, S.; Xia, W.; Gu, X. Molecular Structure and Conformational Design of Donor-Acceptor Conjugated Polymers to Enable Predictable Optoelectronic Property. *Adv. Mater.* **2023**, *35*, 2302178.

(50) Pazmiño Betancourt, B. A.; Douglas, J. F.; Starr, F. W. String model for the dynamics of glass-forming liquids. *J. Chem. Phys.* **2014**, *140*.

(51) Soldera, A.; Metatla, N. Glass transition of polymers: Atomistic simulation versus experiments. *Phys. Rev. E* **2006**, *74*, 061803.

(52) Zhao, H.; Shanahan, J. J.; Samson, S.; Li, Z.; Ma, G.; Prine, N.; Galuska, L.; Wang, Y.; Xia, W.; You, W.; others Manipulating Conjugated Polymer Backbone Dynamics through Controlled Thermal Cleavage of Alkyl Side Chains. *Macromol. Rapid Commun.* **2022**, *43*, 2200533.

(53) Xie, R.; Weisen, A. R.; Lee, Y.; Aplan, M. A.; Fenton, A. M.; Masucci, A. E.; Kempe, F.; Sommer, M.; Pester, C. W.; Colby, R. H.; others Glass transition temperature from the chemical structure of conjugated polymers. *Nat. Commun.* **2020**, *11*, 893.

(54) Ruan, D.; Simmons, D. S. Roles of chain stiffness and segmental rattling in ionomer glass formation. *J. Polym. Sci., Part B: Polym. Phys.* **2015**, *53*, 1458–1469.

(55) Zhang, S.; Ocheje, M. U.; Luo, S.; Ehlenberg, D.; Appleby, B.; Weller, D.; Zhou, D.; Rondeau-Gagné, S.; Gu, X. Probing the viscoelastic property of pseudo free-standing conjugated polymeric thin films. *Macromol. Rapid Commun.* **2018**, *39*, 1800092.

(56) Pei, D.; Wang, Z.; Peng, Z.; Zhang, J.; Deng, Y.; Han, Y.; Ye, L.; Geng, Y. Impact of molecular weight on the mechanical and electrical properties of a high-mobility diketopyrrolopyrrole-based conjugated polymer. *Macromolecules* **2020**, *53*, 4490–4500.

(57) Wang, Y.; Li, Z.; Niu, K.; Xia, W.; Giuntoli, A. A Molecular Dynamics Study of Mechanical and Conformational Properties of Conjugated Polymer Thin Films. *Macromolecules* **2024**,

(58) Cao, Z.; Li, Z.; Zhang, S.; Galuska, L.; Li, T.; Do, C.; Xia, W.; Hong, K.; Gu, X. Decoupling poly (3-alkylthiophenes)'backbone and side-chain conformation by selective deuteration and neutron scattering. *Macromolecules* **2020**, *53*, 11142–11152.

(59) Tsourtou, F. D.; Peristeras, L. D.; Apostolov, R.; Mavrantzas, V. G. Molecular dynamics simulation of amorphous poly (3-hexylthiophene). *Macromolecules* **2020**, *53*, 7810–7824.

(60) Cao, Z.; Leng, M.; Cao, Y.; Gu, X.; Fang, L. How rigid are conjugated non-ladder and ladder polymers? *J. Polym. Sci.* **2022**, *60*, 298–310.

(61) Rubinstein, M.; Colby, R. H. *Polymer physics*; Oxford university press, 2003.

(62) Chen, G.; Dormidontova, E. E. Cyclic vs Linear Bottlebrush Polymers in Solution: Side-Chain Length Effect. *Macromolecules* **2023**, *56*, 3286–3295.

(63) Hsu, H.-P.; Paul, W.; Binder, K. Standard definitions of persistence length do not describe the local "intrinsic" stiffness of real polymer chains. *Macromolecules* **2010**, *43*, 3094–3102.

(64) Zhou, N.; Facchetti, A. Naphthalenediimide (NDI) polymers for all-polymer photovoltaics. *Mater. Today* **2018**, *21*, 377–390.

(65) Park, K. S.; Kwok, J. J.; Dilmurat, R.; Qu, G.; Kafle, P.; Luo, X.; Jung, S.-H.; Olivier, Y.; Lee, J.-K.; Mei, J.; others Tuning conformation, assembly, and charge transport properties of conjugated polymers by printing flow. *Sci. Adv.* **2019**, *5*, eaaw7757.

(66) Zhao, D.; Kim, D.; Ghosh, S.; Wang, G.; Huang, W.; Zhu, Z.; Marks, T. J.; Zozoulenko, I.; Facchetti, A. Mechanical, morphological, and charge transport properties of NDI polymers with variable built-in Π-conjugation lengths probed by simulation and experiment. *Adv. Funct. Mater.* **2024**, *34*, 2310071.

(67) Zhang, Z.; Li, P.; Xiong, M.; Zhang, L.; Chen, J.; Lei, X.; Pan, X.; Wang, X.; Deng, X.-Y.; Shen, W.; others Continuous production of ultratough semiconducting polymer fibers with high electronic performance. *Sci. Adv.* **2024**, *10*, eadk0647.

(68) Schulz, G. L.; Ludwigs, S. Controlled crystallization of conjugated polymer films from solution and solvent vapor for polymer electronics. *Adv. Funct. Mater.* **2017**, *27*, 1603083.

(69) Xu, J.; Wang, S.; Wang, G.-J. N.; Zhu, C.; Luo, S.; Jin, L.; Gu, X.; Chen, S.; Feig, V. R.; To, J. W.; others Highly stretchable polymer semiconductor films through the nanoconfinement effect. *Science* **2017**, *355*, 59–64.

(70) Cohen, A. E.; Jackson, N. E.; De Pablo, J. J. Anisotropic coarse-grained model for conjugated polymers: Investigations into solution morphologies. *Macromolecules* **2021**, *54*, 3780–3789.

TOC Graphic

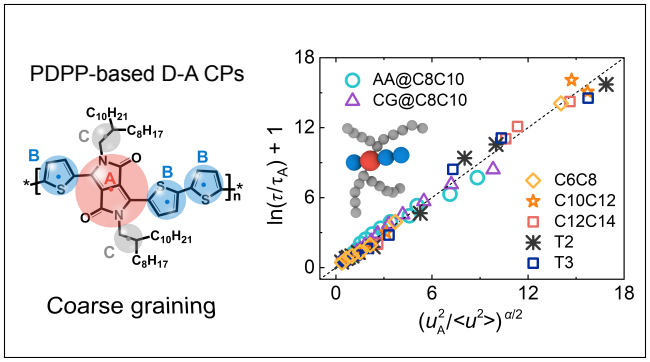
PDPP-based D-A CPs
Coarse graining
AA@C8C10
CG@C8C10
C6C8
C10C12
C12C14
T2
T3
18
12
6
0
0
6
12
18
ln(τ/τA) + 1
(u2A/<u2>)α/2